Article

# Bi-Magnetic Iron(III) Oxide Nanocrystals Embedded in MCM-41 Mesoporous Silica

S. J. Stewart,[*,†,‡] A. F. Cabrera,[†] N. A. Fellenz,[§] R. C. Mercader,[†] J. F. Bengoa,[||] and S. G. Marchetti[||]

[†]IFLP-CCT- La Plata-CONICET and Departamento de Física, Facultad de Ciencias Exactas, C. C. 67, Universidad Nacional de La Plata, 1900 La Plata, Buenos Aires, Argentina

[‡]Instituto Ciencias de la Salud, Universidad Nacional Arturo Jauretche, Avenida Calchaquí 6200, 1888 Florencio Varela, Buenos Aires, Argentina

[§]Universidad Nacional de Rio Negro, CONICET, Belgrano 526, 8500 Viedma, Rio Negro, Argentina

[||]Departamento de Química, Facultad de Ciencias Exactas, Universidad Nacional de La Plata, CONICET, CINDECA, CICPBA, 47 No 257, 1900 La Plata, Buenos Aires, Argentina

ABSTRACT: This is a study on the magnetism of a Fe_2O_3@MCM-41 composite made up of iron(III) oxide nanocrystals of average length size of 4 nm embedded in the channels of a MCM-41 mesoporous matrix. Through Mössbauer spectroscopy, X-ray absorption experiments and static and dynamic magnetic measurements, we identify the guest iron oxide entities as composed by exchange-coupled hematite (weak ferromagnetic WF) and maghemite (ferrimagnetic FiM) arranged in a string of beads configuration. The WF/FiM nanocrystals behave as independent particle moments that block as a whole below $T_B = 17$ K. The log-normal energy barrier distribution function determined from relaxation measurements shows a maximum at an energy $E = 200$ K. We explore to what extent the contact between domains of the two coexisting oxides controls the magnetism of this biphasic nanosystem.
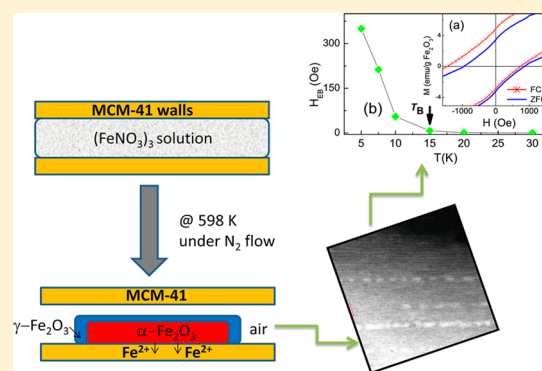
I. INTRODUCTION

Bicomponent nanoparticles combining compounds with different magnetic phases are attracting increasing attention to develop systems able to retain or enhance the properties and functionalities of their individual counterparts in the quest for diverse technological applications and materials with novel properties.[1−9] The careful choice of compounds with different structures and compositions leads to systems that are not simply the result of the added components properties but also due to the role of the interface coupling as well as the interactions between the coexisting phases.

More than a decade ago Shumrykev et al.[10] found that the superparamagnetic limit can be significantly improved by means of systems containing interfaces of ferromagnetic/antiferromagnetic (FM/AF) phases. Lately this has produced a flurry of different synthesizing methods that have been attempted to obtain bimagnetic nanoparticles, i.e., no matter how small they are, the synthesis purposely includes FM/AF or other interfaces combining materials with different magnetic order and anisotropy into the effective magnetic properties of a single nanoparticle.[5]

Recently, one approach that has been attempted many times is the synthesis of core/shell bimagnetic nanoparticles.[3−9] Along this line, several efforts are being devoted to the investigation of bimagnetic nanocrystals where at least one of its components is an iron oxide (ferrimagnetic (FiM)), like γ-Fe_2O_3 or Fe_3O_4, and AF like α-Fe_2O_3 or FeO.[2,7−9]

Bicomponent iron oxide nanoparticles (IONPs), where one phase is derived from the other, usually (but not necessarily) forming a core−shell configuration that can be obtained by thermal decomposition of precursors or by performing a controlled treatment (oxidation or reduction) of the particle surface.[2,5,7] Obviously, toward the tuning of the overall properties of bicomponent nanosystems, this does not essentially need to be accomplished by an entity with the shape of a magnetic nanoparticle. Other structures at the nanoscale, like nanowires, nanorods or nanotubes, can display magnetic moments stabilized by interaction at the interfaces.

Taking into account that recent publications[4] have found that there is a competition between the core and shell of self-supported nanoparticles that show their magnetism altered because of the size confinement, we set about to synthesize nanoparticles confined not by their own size but by embedding the iron oxides in the diamagnetic regular array of nano-channels with amorphous SiO_2 walls exhibited by MCM-41.[11,12]

In addition to synthesizing a better magnetic material, from the point of view of basic studies in magnetism, which currently lack an inclusive theory for the behavior of nanoparticle systems— the confinement of IONPs in MCM-41 is a

A

convenient strategy to obtain a model system of weakly interacting IONPs arranged in a regular quasi 1D-configuration. Furthermore, if the confinement of IONPs is attained by thermal decomposition of precursors, this can be an approach to synthesize nanocrystals composed by iron oxide phases that are interconnected.

Previous works on Fe (III) oxide-containing MCM-41 that included magnetic characterizations[13−18] have reported that the nanocomposites present enhanced magnetic properties and superparamagnetic behavior. It has also been found that, depending on the fabrication conditions and metal loading levels, hematite (α-Fe_2O_3), maghemite (γ-Fe_2O_3), or mixtures of these oxides have been detected as part of the composites,[13−18] but a detailed characterization of their magnetic properties has not yet been reported.

In this work we report a study on IONPs composed by exchange-coupled hematite and maghemite-like species embedded in the mesoporous extremely regular channels of a MCM-41 matrix. Because our nanoparticles ended up with sizes about 1 order of magnitude smaller than usually found in the literature, their magnetic behavior was worth studying in detail. The properties and tentative explanation for the magnetic behavior of this bimagnetic supported system are described in detail in this manuscript.

II. EXPERIMENTAL SECTION

The MCM-41 support was prepared following the procedure proposed by Ryoo et al.[19] The Fe_2O_3@MCM-41 composite was obtained by impregnation with an aqueous solution of $Fe(NO_3)_3 \cdot 9H_2O$, and then the sample was dried in air and afterward calcined under dry N_2 flow (60 cm^3/min, 5 ppm of O_2). Details of sample preparation and morphological characterization can be found elsewhere.[20] The composite was characterized by low-angle X-ray diffraction XRD (Cu $K\alpha$). The iron content determined using absorption atomic spectroscopy was 4.6% (w/w).

Mössbauer spectra were recorded at room temperature and 4.2 K with a conventional transmission spectrometer using a ^{57}Co source in a Rh matrix moved via triangular velocity wave. The isomer shift (δ) is given relative to Fe metal at room temperature.

Near-edge X-ray absorption fine structure (XANES) and extended X-ray absorption fine structure (EXAFS) spectra at the Fe K-edge (7112 eV) were recorded at room temperature in transmission mode using a Si (111) monochromator at the XAS beamline of the LNLS (Laboratorio Nacional de Luz Sincrotron) in Campinas, Brazil. The spectra analysis was performed by pre-edge background subtraction followed by a normalization procedure considering the extended region. The fine structure oscillations $\chi(k)$ of each spectrum in the extended region were isolated using the ATHENA program[21] and Fourier transformed over a specific k range. Absorption spectra of bulk hematite (α-Fe_2O_3) and maghemite (γ-Fe_2O_3) were also registered.

DC magnetic measurements were carried out using a MPMS (Quantum Design) and a vibrating sample magnetometer VSM (Lakeshore 7404). The zero-field cooling (ZFC) magnetization curves were measured cooling the sample from ambient down to 4 K, applying a magnetic field H_{FC} and recording the magnetization on warming. The field-cooling FC curves were obtained by measuring the magnetization on warming after the sample was cooled from room temperature with an applied H_{FC}. $M−H$ hysteresis loops were measured at different temperatures within the 5 to 300 K range using a maximum applied field H = 50 kOe. Hysteresis loops under FC-condition were also measured. The AC susceptibility measurements between 13 and 325 K were taken in a LakeShore 7130 susceptometer using field amplitude of 1 Oe and frequencies in the 50 Hz to 10 kHz range.

Thermoremanent magnetization (TRM) measurements were performed cooling the sample to the chosen temperature under applied fields H = 0.2 and 2 kOe. After stabilizing the temperature, the field was switched off, and the magnetization was measured as a function of time. After completion of each measurement, the sample was heated up to 200 K in zero field, and then field-cooled again to a new temperature.

III. RESULTS AND DISCUSSION

Results from XRD, X-ray Absorption and Mössbauer Spectroscopy. The impregnation of MCM-41 support and later decomposition of the inorganic iron salt gave rise to an ordered configuration of nanocrystals that preserves the hexagonal structure of the mesoporous solid, as shown by low-angle XRD results (Figure 1). Because of the low Fe
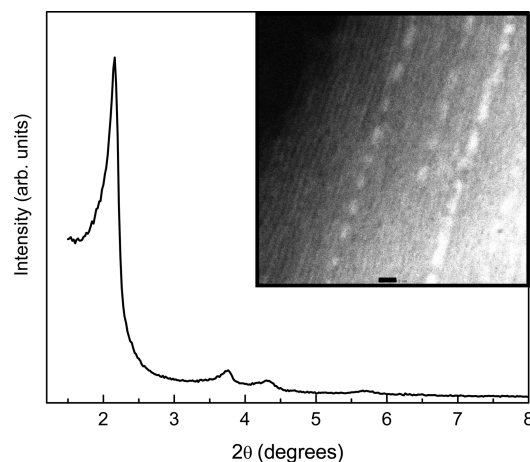

Figure 1. XRD patterns of the Fe2O3@MCM-41 composite. Inset: STEM-HAADF image of the composite (reproduced from ref 20 with permission of Elsevier © 3727670376045). The bar scale corresponds to 5 nm.

content of the solid and the very small size of the nanoparticles, it was impossible to sort out the XRD diffraction peaks at higher angles of the Fe oxides from the signal originated in the amorphous SiO_2 walls of the MCM-41 matrix.

Images from scanning transmission electron microscopy high-angle annular dark-field (STEM-HAADF) allowed a direct observation of iron oxide nanocrystals of average length size of 4 nm inside the channels (see Figure 1 inset and ref 20). It is worth noticing that not all the MCM-41 channels contain nanoparticles and that the channel filling is partial. Further, each pore containing nanocrystals has its next-neighbor channels empty. The resulting configuration can be depicted as an arrangement of a string of nanocrystals with a log-normal distribution of sizes of average length $L \sim 4$ nm confined inside the MCM-41 channels with a diameter of about 3 nm.[20] The estimated average distance between iron-containing nanocrystals along the same channel is about $d = 4$ nm.

Figure 2 shows the Fe K-edge XANES spectra of Fe_2O_3@ MCM-41 composite and of standard references (bulk hematite α-Fe_2O_3 and maghemite γ-Fe_2O_3). The spectrum displays a

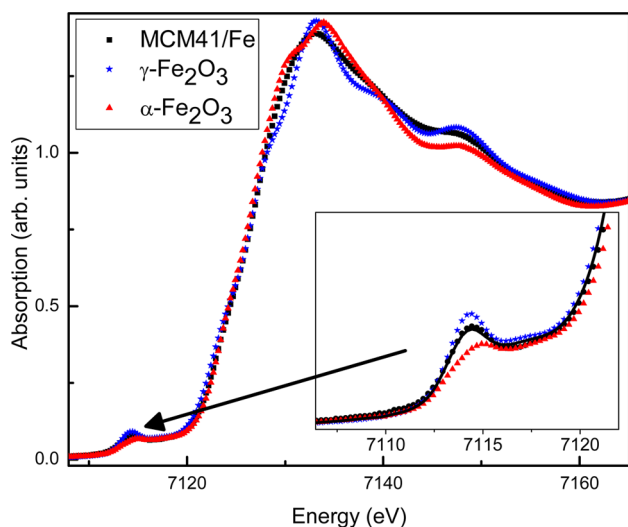**Figure 2.** XANES spectra at the Fe K-edge of Fe_2O_3@MCM-41, bulk hematite α-Fe_2O_3, and bulk maghemite γ-Fe_2O_3. The solid line (inset) represents the linear combination of α-Fe_2O_3, and γ-Fe_2O_3 spectra in about 50:50 ratio.

pre-edge structure (1s → 3d and 1s → 3d/4p electronic transitions) whose intensity is higher than the intensity registered for α-Fe_2O_3 but lower than the γ-Fe_2O_3 one. The edge energy is compatible with a +3 oxidation state of iron. After the absorption edge, the main-edge crest at 7132 eV (1s → 4p transition) is less resolved, and the peaks are broader than those of α-Fe_2O_3 and γ-Fe_2O_3. The near edge peak structure can be reproduced satisfactorily assuming a linear combination of the reference spectra α-Fe_2O_3 and γ-Fe_2O_3 in almost equal percentages (Figure 2).

Figure 3 shows the Fourier Transform (FT) of the EXAFS oscillations corresponding to Fe_2O_3@MCM-41 composite and
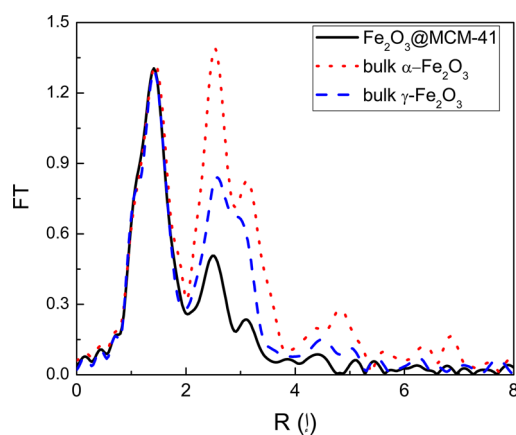

Figure 3. Fourier transform (FT) of the $k^2\chi(k)$ EXAFS functions.

bulk α-Fe_2O_3 and γ-Fe_2O_3. The first FT peak corresponds to the oxygen first coordination shell, and its intensity is comparable to the iron oxides used as references. By contrast, the second peak has a rather low intensity. This result reflects the disorder due to the small particle size that alters the second shell of the central Fe atom in an iron oxide structure.

The Mössbauer spectrum at room temperature (RT) (not shown) consisted of a broad doublet signal with a δ = 0.34 mm/s and a quadrupole splitting Δ = 0.70 mm/s, which reflects the superparamagnetic (SPM) relaxation state of the oxide

particles. The 4.2 K spectrum (Figure 4) exhibits magnetic signals of iron oxide particles that are in a blocked state. The
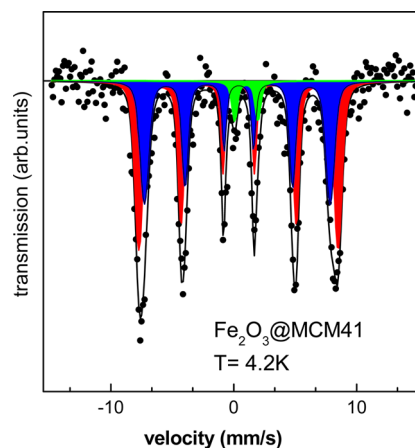

Figure 4. Mössbauer spectrum taken at 4. 2K. The solid line (black) is the result of the fitting described in the text. The red, blue and green marked areas correspond to sextet I, sextet II and the doublet, respectively.

latter was fitted assuming two Fe^{3+} broad sextets, sites I and II, plus a Fe^{2+} doublet. Their hyperfine parameter values allow us assigning the sextet I to α-Fe_2O_3 in weak ferromagnetic (WF) state whose Morin transition has been suppressed,[22] and the sextet II as belonging to unresolved A and B-spinel sites in maghemite-like nanoparticles.[23] The minor doublet at 4.2 K corresponds to paramagnetic iron(II) ions probably migrated into the channel walls of the MCM-41 matrix.[24] The presence of a paramagnetic component is also detected in the magnetic response (see below).

Magnetic Properties of Fe_2O_3@MCM-41 Composite. Figure 5 shows the thermal dependence of the DC magnet-
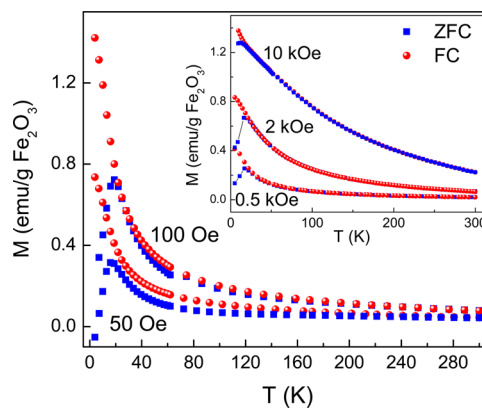

Figure 5. Zero field cooling (ZFC) and field cooling fields (FC) curves under cooling fields H_{FC} of 50 and 100 Oe. Inset: ZFC-FC curves under H_{FC} of 0.5, 2, and 10 kOe.

ization of Fe_2O_3@MCM-41 composite taken under ZFC-FC conditions, under low cooling fields (H_{FC} = 50 and 100 Oe). The data show the magnetization typical of single-domain particles characterized by a SPM regime at high temperatures. The ZFC magnetization measured under the 50 Oe-field shows a rather sharp maximum at about T_B = 17 K, which represents the blocking (or freezing) temperature of particle (or spin-disordered) moments. Assuming that the particles are non-

interacting and have uniaxial anisotropy, an average barrier energy of about 420 K can be roughly estimated from $E_A \approx 25 k_B T_B$, where an attempting time $\tau_0 \sim 10^{-9}$ s was considered.[25] In case the interparticle interaction cannot be neglected, this T_B value could be higher than what might be granted by the average anisotropy of the nanoparticles. In contrast to the ZFC curve, the FC magnetization continuously increases as the temperature decreases. This trend continues below T_B and indicates the weak strength of the magnetic interparticle interactions as the moments align along the 50 Oe applied field. We observe that the ZFC and FC curves superimpose at high temperatures, as expected for moments in an equilibrium state. However, the remaining irreversibility slightly above T_B indicates the existence of a distribution of energy barriers. The ZFC−FC curves were also measured under higher fields H_{FC} = 0.5, 2, and 10 kOe (Inset Figure 5). T_B shifts toward lower values as H_{FC} increases (T_B = 12 K for the highest H_{FC}) due to the effect of the external magnetic field on the energy barriers.[25] At these fields the irreversibility persists but only below T_B. The high-field ZFC curve (H_{FC} = 10 kOe) follows a Curie−Weiss like behavior at high temperatures, but still shows a downward curvature below 15 K. The latter indicates that, in spite of the weak magnetic interactions, the frozen magnetic state achieved by the system inhibits a complete alignment of the moments along the 10 kOe-field at low temperature.

The M−H hysteresis loops taken at temperatures in the 5−300 K range are shown in Figure 6. These data were analyzed
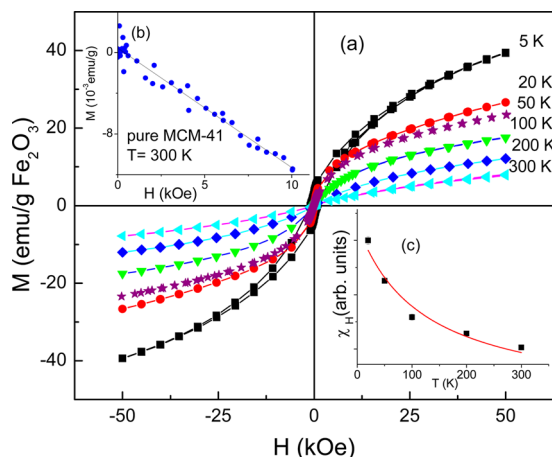

Figure 6. (a) Hysteresis cycles at the temperatures shown using a maximum applied magnetic field H = 50 kOe. (b) The inset shows the magnetization as a function of the applied magnetic field of pure MCM-41 measured at 300 K. (c) The inset shows the high-field susceptibility as a function of temperature. The solid line corresponds to the Curie−Weiss curve fitting.

after discounting the diamagnetic contribution from the MCM-41 matrix, whose susceptibility is $\chi_d = -1.2 \times 10^{-6}$ emu·g^{-1}·Oe^{-1} (see inset Figure 6). On one hand, we observe that the loops measured at 300, 200, and 100 K do not show hysteresis. These cycles were best fitted considering a SPM contribution M_{SPM} (Langevin function) and a linear paramagnetic contribution $M_{PM} = \chi_H H$. The results show that the high-field susceptibility, χ_H, follows a Curie−Weiss relationship (inset Figure 6). On the other hand, an effective particle magnetic moment $\mu_{eff} \sim 850$ μ_B can be estimated from the fitting results. In the case of WF hematite, the particle magnetic moment

comes from the existence of a small spontaneous moment whose total contribution depends on the particle size as well as the disorder of the surface or interfacial region. For AF hematite, the particle moment value results from uncompensated surface spins. Therefore, a variety of average μ values can be found in the literature for α-Fe$_2$O$_3$ dispersed in different matrices. For instance, a particle magnetic moment of 300 μ_B was estimated for 7 nm-hematite nanoparticles embedded in mesoporous silica SBA-15.[26] On the other hand, μ values of about 120 and 980 μ_B were reported for α-Fe$_2$O$_3$/SiO$_2$ nanocomposites with particles of average sizes of 4 and 10 nm, respectively.[27] On the other side, the magnetic moment per γ-Fe$_2$O$_3$ particle depends on its size, surface disorder, and the order−disorder characteristics of the sample.[28] In the case of γ-Fe$_2$O$_3$/SiO$_2$ nanocomposites, the saturation magnetization is commonly rather below the reported value for bulk γ-Fe$_2$O$_3$ (74 emu/g) and slightly lower than the values measured in γ-Fe$_2$O$_3$ particles of similar sizes.[28−30] As an example, effective μ values from 220 to 370 μ_B have been reported for 4 to 4.8 nm γ-Fe$_2$O$_3$ in mesoporous SBA-15 silica,[31] while this value can be about 7000 μ_B for acid oleic-coated γ-Fe$_2$O$_3$ nanoparticles of 7 nm.[32] In our case, the μ_{eff} value reflects the contribution from both oxides having unpredictable saturation magnetizations due to the very small particle sizes.[33]

The $\mu_{eff} \sim 850$ μ_B implies a dipolar interparticle interaction energy $E_{dip} \sim 0.03$ meV considering an average distance of 4 nm between the intrachannel particles. This can result in a dipolar-driven freezing of the particle moments below a critical temperature $E_{dip}/k_B = T_0 = 0.3$ K, i.e., far below the temperature where the blocking processes take place. For that reason, it is expected that the influence of interparticle dipolar interactions on T_B is negligible. Thus, the weakly interacting magnetic nanoparticles synthesized in this work constitute an almost ideal model system to study the magnetic properties of a regular quasi 1D-configuration.

We observe that the loops registered at 5 and 20 K display hysteresis (Figures 6 and 7a) with coercive fields of about 20 and 900 Oe, respectively. They show a rapid increase of the magnetization at low fields (up to ≈2 kOe) and curve downward at higher fields without reaching the complete saturation for fields up to 50 kOe. These hysteresis cycles were well reproduced considering two contributions: (i) a ferromagnetic component[34] M_{FM} and (ii) a paramagnetic one M_{PM} (Brillouin function). On one hand, an effective moment of about 3.9 μ_B per iron ion results for the paramagnetic phase, which is characteristic of low spin iron(II). This can be associated with those iron ions diffused into the MCM-41 walls, in agreement with Mössbauer results. On the other hand, the FM component has a saturation magnetization M_S = 7.7 emu per gram of Fe$_2$O$_3$ at 5 K. This value arises from the superposition of both nanosized hematite (WF) and maghemite (ferrimagnetic FiM) phases that form the nanocrystals. As mentioned before, the reduced M_S for nanosized γ-Fe$_2$O$_3$ and the enhanced M_S reported for α-Fe$_2$O$_3$ nanoparticles with respect to their bulk values[27] hinder an unambiguous estimation of the hematite to maghemite ratio from the M−H data.

Hysteresis loops were also recorded at different temperatures after field cooling the sample from room temperature under a cooling field H_{FCool} = 50 kOe (Figure 7a). A loop shift reflects the existence of an exchange anisotropy due to the coexistence of ferromagnetic (FM or FiM) and AF phases, disordered/AF, or disordered/FM phases with interfacial interactions.[35,36] In
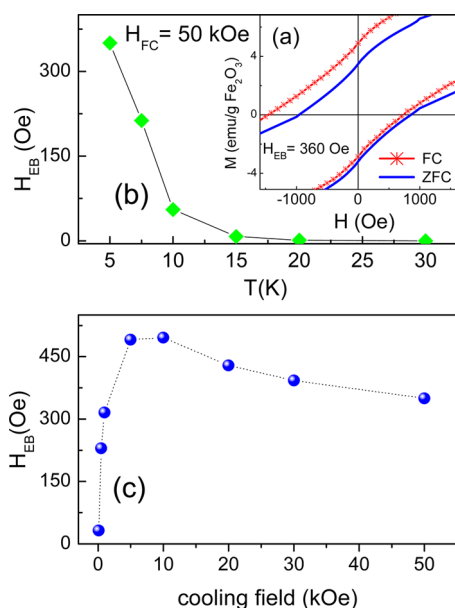
Figure 7. (a) Low-field regions of $M-H$ loops at $T = 5$ K taken under ZFC and FC conditions with $H_{FC} = 50$ kOe, (b) Exchange bias field (H_{EB}), as a function of temperature under a cooling field $H_{FC} = 50$ kOe. (c) Exchange bias field for different cooling fields. Lines are a guide for the eyes.

our case, we observe a shift to negative fields when the loops were measured below 20 K, i.e., once the blocking/freezing of moments has taken place. The exchange bias field (H_{EB}), defined as $H_{EB} = (|H_{CR}| - |H_{CL}|)/2$, where H_{CR} and H_{CL} are the right and left coercive fields, respectively, measured at different temperatures is shown in Figure 7b. This shift can be attributed to the exchange anisotropy due to the presence of the two interconnected iron oxide phases, i.e., a WF core (hematite) and a FiM surface (maghemite).

Figure 8 shows the results of the AC-susceptibility measurements. The in-phase susceptibility component, χ', shows a maximum at a temperature T_{max} ($T_{max} \sim 22$ K for a frequency $f = 48$ Hz) that coincides with the occurrence of the turning point of the out-of-phase component, χ''. Also, χ''
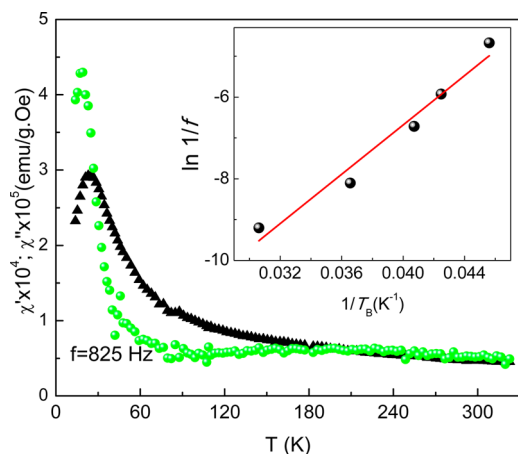

Figure 8. In-phase (χ', triangles) and out-of-phase (χ'', circles) components of the AC susceptibility measured with a frequency of 825 Hz. Inset: Néel−Arrhenius plot showing the experimental time ($\ln t$) vs the inverse of the blocking temperature (T_B^{-1}) from the AC-susceptibility measurements.

shows a maximum. When increasing the frequency, T_{max} shifts to higher temperatures and χ' decreases. To quantify the frequency shift the empirical parameter p is commonly reported, which gives the relative shift of temperature $\Delta T_{max}/T_{max}$ per decade of frequency.[37] In our case, the $p = 0.12$ value lies between the values usually found for independent particle SPM systems.[37] A Néel-Arrhenius plot for the multifrequency AC-susceptibility is shown in the inset of Figure 8. The linear fit gives reasonable values for the attempting time $\tau_0 = 5.6 \times 10^{-9}$ s and for an energy barrier $E_A = 300$ K, assuming a relaxation time $\tau = \tau_0 : \exp(E_A/k_B T)$. This result would indicate that the particles are predominantly noninteracting. Considering the particles' dimensions and assuming that they fill the pore diameters, we can roughly estimate an anisotropy constant $K \sim 1.5 \times 10^6$ erg·cm^{-3} for uniaxial nanoparticles. This value is increased with respect to the magnetocrystalline anisotropy of bulk maghemite (4.7×10^4 erg·cm^{-3}) or bulk hematite (8×10^4 erg·cm^{-3}).[27,30] However, it has been found that these effective K values for α-Fe$_2$O$_3$ and γ-Fe$_2$O$_3$ increase one or 2 orders of magnitude with decreasing particle size due to the growth of the surface contribution.[27,30] For instance, a $K_{eff} = 1.6 \times 10^6$ erg·cm^{-3} has been reported for α-Fe$_2$O$_3$ nanoparticles dispersed in silica.[27]

All the results point toward two iron-oxide species taking part in the Fe$_2$O$_3$@MCM-41 composite, i.e., hematite and maghemite in a ratio of about 1.3 roughly estimated from Mössbauer results (Figure 9 and Table 1). It is expected that
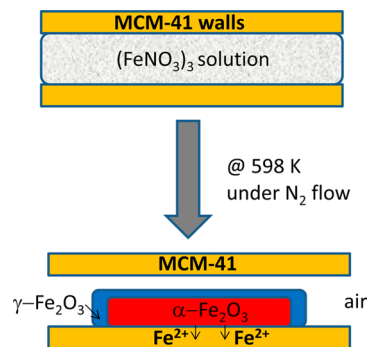

Figure 9. Schematic drawing of the synthesis procedure to obtain a two-component (hematite and maghemite) Fe$_2$O$_3$@MCM-41 composite.

Table 1. Hyperfine Parameters Obtained by Fitting the 4.2 K Mössbauer Spectrum[a]

component	δ (mm/s)	2ε (mm/s)	B_{hf} (T)	area (%)
Sextet I	0.47(1)	0.02(1)	50.3(1)	54(2)
Sextet II	0.43(1)	0.12(2)	46.9.(1)	41(2)
PM Fe^{2+}	1.10(3)	1.90(6)	-	5(1)

[a]2ε is the quadupole splitting, B_{hf} is the hyperfine field. Isomer shifts δ refer to α-Fe at room temperature.

once some of the MCM-41 channels are partially filled with Fe(NO$_3$)$_3$·9H$_2$O after impregnation, hematite nanocrystals form favored by the rapid thermal decomposition of the iron inorganic salt at temperatures higher than 250 °C.[38] However, as the thermal treatment is carried out under low oxygen partial pressure (N$_2$ flow), the α-Fe$_2$O$_3$ nanocrystals would start losing surface O^{2-} ions, while surface Fe^{3+} ions would be transformed to Fe^{2+} to keep the lattice neutrality giving rise to a structurally modified superficial layer. It is known that Fe^{2+} ions have a

strong tendency to produce a surface iron silicate phase.[23] Therefore, a low percentage of Fe^{2+} ions probably migrate into the MCM-41 walls and give rise to the paramagnetic component. When the sample is re-exposed to air under ambient conditions, an oxidation likely takes place on the superficial layer of the nanocrystals, and the iron ions return to their +3 valence state and form a maghemite-like phase instead of recovering the hematite structure due to the insufficient annealing energy to produce the spinel (maghemite) to corundum (hematite) structural change.[39] As a result, our iron(III) oxide nanocomposite consist of WF α-Fe_2O_3 core layered by FiM maghemite-like phase, and all the α-Fe_2O_3/γ-Fe_2O_3 nanocrystals arrange forming a string of beads structure inside the MCM-41 channels (inset Figure 1).

Bimagnetic System: Exchange Anisotropy and Magnetic Viscosity. The above-described configuration provides a model system of exchange-coupled WF/FiM nanocrystals with negligible interparticle interactions worth being investigated from the viewpoint of magnetism. To further characterize the exchange anisotropy that gives rise to the loop shift, we have obtained $M–H$ curves at 5 K after field-cooling the samples under various fields H_{FCool} (Figure 7c). In these cases, once the 5 K temperature is achieved, the field was removed and the loop recorded. We observe that H_{EB} increases with the cooling field up to H_{FCool} = 5 kOe, where it reaches a value of about 0.5 kOe. H_{EB} maintains almost this value for H_{FCool} = 10 kOe and then decreases monotonically for H_{FCool} higher than 10 kOe (Figure 7c). Similar behaviors have been observed in nanosystems with interfacial exchange coupling between coexisting magnetic phases.[36,40] This has been interpreted as the existence of energy competition among the exchange interactions among the spins located at the interfaces and the Zeeman energy established by H_{FCool}. In our case, as H_{FCool} increases up to 5 kOe, the exchange anisotropy dominates below T_B, and the loops are shifted. On the contrary, for cooling fields higher than 10 kOe the Zeeman energy overcomes the anisotropy energy, and therefore H_{EB} decreases.

The inset of Figure 10 shows the TRM magnetization vs relaxation time measured after cooling with H = 0.2 kOe at some representative temperatures. A similar behavior was obtained with H = 2 kOe (not shown). These curves were fitted following the expression

$$M(t) = M_0 - S(T)\cdot\ln(t/\tau_0) \qquad (1)$$

where M_0 is the initial magnetization, $S(T)$ is the magnetic viscosity, and τ_0 is the characteristic relaxation time.[41,42] We found a τ_0 value of about 10^{-9} s, which lies within the range expected for small-particle systems.[42] The thermal dependence of S (Figure 10) shows a maximum at about T_S = 13 and 10 K for measurements with H = 0.2 and 2 kOe, respectively, i.e., not far from the range of T_B estimated from the thermal dependence of the magnetization. The proximity between T_S and T_B reinforces our previous observation that interparticle interaction effects are negligible and do not influence the relaxation behavior.[43] Below T_S the $S(T)$ behavior can be assumed as $S = k_BT/U$, with U being the average energy barrier.[42] A linear fit gives $U \sim$ 290 and 400 K for 0.2 and 2 kOe, respectively, values that lie within the range of the effective energy barriers E_A previously determined.

Since the energy barrier is given by the product between the anisotropy constant K and the particle volume V, and these variables are both distributed in real systems, it can be better characterized by a distribution of barriers. Information concerning this distribution can be obtained from the relaxation measurements by applying the $T\cdot\ln(t/\tau_0)$ scaling method.[44] This scaling allows extrapolating the TRM behavior to experimentally inaccessible times by bringing all the data in a unique master curve.[45] The energy distribution function $n(E)$ can be obtained by performing the time derivative of the scaling curve.[44,45] In our case, the resulting scaling considering $\tau_0 = 10^{-9}$ s is shown in Figure 11a. The master curve is generally
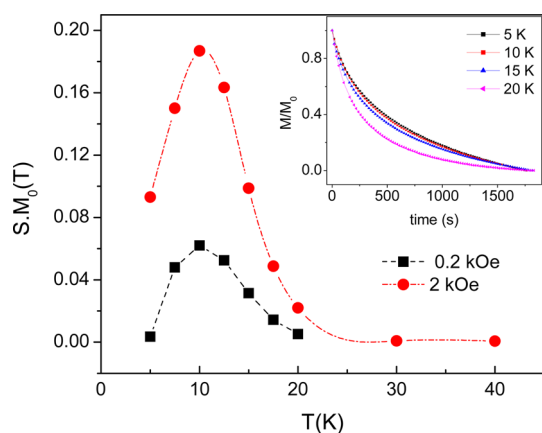
Figure 11. (a) Magnetization as a function of the scaling variable for 0.2 and 2 kOe cooling fields. (b) Energy barrier distribution $n(E)$ obtained by differentiating the magnetization with respect to the ln t.

Figure 10. Magnetic viscosity S obtained by curve fitting the TRM. Inset: Time dependence of the normalized magnetic moment after cooling with 0.2 kOe applied magnetic field at several representative temperatures.
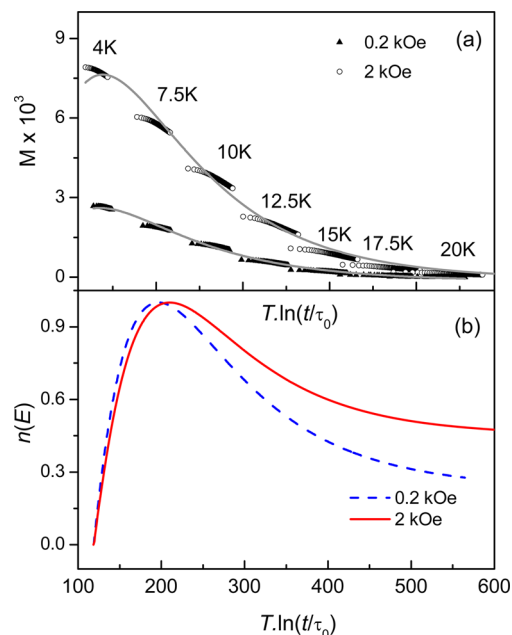
reproduced assuming a log-normal distribution of energy barriers. The inverse of the derivative of the remnant magnetization as a function of the activation energy $T\cdot\ln(t/\tau_0)$ gives the energy barrier distribution (see Figure 11b). The distribution shows a maximum at about 200 K for both cooling fields. The fact that this value is below the average energy barriers estimated above assuming thermal activated processes

can be attributed to the different magnetic sizes involved in each measurement.

The magnetic guest inside the MCM-41 channels consists of two types of iron(III) oxide nanoparticles, which behave superparamagnetically at ambient conditions. In spite of the existence of two magnetic species WF and FiM, the nanocrystal moments gradually block as a whole, showing a unique blocking temperature and rather smooth hysteresis loops. The system shows some features typical of independent particle moments: the relaxation time is described by the Néel−Arrhenius equation, the dependence of T_B with the experimental window time corresponds to a thermal activated process, the FC magnetization follows the low-field alignment and the temperature at which the maximum of the viscosity occurs is close to T_B. On the other hand, the intimate contact between the magnetic phases gives rise to the shifted loops that reflect the interfacial spin coupling between the WF phase and the FiM one. The string of beads configuration of separated two-component particles, jointly with the magnitude of the particle moments, guarantee the low influence of interparticle interactions in their magnetic behavior. The interface region probably exhibits a certain degree of disorder due to the small particle sizes. As the maghemite-like shell originates from a partial reduction of hematite nanoparticles, it is not surprising that there exists a compositional gradient in the interfacial region. The fact that the exchange anisotropy manifests below T_B, indicates that the blocking also involves the blocking or freezing of moments located at the interfacial zones. Once the spins at the interfacial region freeze and act as a pinning, the two magnetic phases remain magnetically connected, and the system behaves as a whole.

IV. CONCLUSIONS

The structural features of iron(III) oxide nanoparticles hosted inside the pores of MCM-41 have been determined by combining Mössbauer and X-ray absorption spectroscopies jointly with STEM-HAADF and magnetic measurements. The iron(III) oxide nanocrystals of average length size of about 4 nm are embedded in MCM-41 channels of 3 nm diameter displaying an arrangement like a string of beads characterized by an uneven filling. The nanocrystals are composed by interconnected hematite and maghemite-like phases. The hematite phase is in a WF state, while the FiM response of the composite mainly comes from maghemite.

The particular array inside the channels inhibits the influence of interparticle interactions on the blocking and relaxation processes of particle moments. The WF/FiM nanocrystals behave as a whole during the blocking process. An average blocking temperature of about 17 K can be inferred from DC magnetization. The shifted loops observed below T_B reveal the exchange anisotropy throughout the spin moments at the interfacial WF and FiM regions. Applied fields of 10 kOe are strong enough to produce the Zeeman energy necessary to overcome the exchange coupling between WF and FiM phases. The temperature dependence of the viscosity shows a maximum close to the blocking temperature. The log-normal energy barrier distribution function obtained from the relaxation measurements shows a maximum at energy of 200 K.

AUTHOR INFORMATION

Notes

The authors declare no competing financial interest.

REFERENCES

(1) Lee, J.-H.; Jang, J.; Choi, J.; Moon, S. H.; Noh, S.; Kim, J.; Kim, J.-G.; Kim, I.-S.; Park, K. I.; Cheon, J. Exchange-coupled Magnetic Nanoparticles for Efficient Heat Induction. *Nat. Nanotechnol.* **2011**, *6*, 418−422.

(2) Sytnyk, M.; Kirchschlager, R.; Bodnarchuk, M. I.; Primetzhofer, D.; Kriegner, D.; Enser, H.; Stangl, J.; Bauer, P.; Voith, M.; Hassel, A. W.; et al. Tuning the Magnetic Properties of Metal Oxide Nanocrystal Heterostructures by Cation Exchange. *Nano Lett.* **2013**, *13*, 586−593.

(3) Wetterskog, E.; Tai, J.; Grins, Ch-W.; Bergström, L.; Salazar-Alvarez, G. Anomalous Magnetic Properties of Nanoparticles Arising from Defect Structures: Topotaxial Oxidation of $Fe_{1−x}O|Fe_{3−\delta}O_4$ Core|Shell Nanocubes to Single-Phase Particles. *ACS Nano* **2013**, *7*, 7132−7144.

(4) Medeiros Filho, F. C.; Oliveira, L. L.; Pedrosa, S. S.; Rebouças, G. O. G.; Carriço, A. S.; Dantas, A. L. Impact of Core-Shell Dipolar Interaction on Magnetic Phases of Spherical Core-Shell Nanoparticles. *Phys. Rev. B: Condens. Matter Mater. Phys.* **2015**, *92*, 064422−064428.

(5) López-Ortega, A.; Estrader, M.; Salazar-Alvarez, G.; Roca, A. G.; Nogués, J. Applications of Exchange Coupled Bi-magnetic Hard/Soft and Soft/Hard Magnetic Core/Shell Nanoparticles. *Phys. Rep.* **2015**, *553*, 1−32.

(6) Vasilakaki, M.; Trohidou, K. N.; Nogués, J. Enhanced Magnetic Properties in Antiferromagnetic-Core/Ferrimagnetic-Shell Nanoparticles. *Sci. Rep.* **2015**, *5*, 9609.

(7) Chen, Ch-J.; Chiang, R.-K.; Lai, H.-Y.; Lin, Ch-R. Characterization of Monodisperse Wustite Nanoparticles following Partial Oxidation. *J. Phys. Chem. C* **2010**, *114*, 4258−4263.

(8) Sun, X.; Frey Huls, N.; Sigdel, A.; Sun, S. Tuning Exchange Bias in Core/shell FeO/Fe_3O_4 Nanoparticles. *Nano Lett.* **2012**, *12*, 246−251.

(9) Hai, H. T.; Kura, H.; Takahashi, M.; Ogawa, T. Phase Transformation of FeO/Fe_3O_4 Core/shell Nanocubes and Facile Synthesis of Fe_3O_4 Nanocubes. *J. Appl. Phys.* **2010**, *107*, 09E301−09E301−3.

(10) Skumryev, V.; Stoyanov, S.; Zhang, Y.; Hadjipanayis, G.; Givord, D.; Nogues, J. Beating the Superparamagnetic Limit with Exchange Bias. *Nature* **2003**, *423*, 850−853.

(11) Cai, Q.; Lin, W.; Xiao, F.; Pang, W.; Chen, X.; Zou, B. The Preparation of Highly Ordered MCM-41 with Extremely Low Surfactant Concentration. *Microporous Mesoporous Mater.* **1999**, *32*, 1−15.

(12) Dapurkar, S. E.; Badamali, S. K.; Selvam, P. Nanosized Metal Oxides in the Mesopores of MCM-41 and MCM-48 Silicates. *Catal. Today* **2001**, *68*, 63−68.

(13) Zhang, L.; Papaefthymiou, G. C.; Ying, J. Y. Synthesis and Properties of γ-Fe_2O_3 Nanoclusters within Mesoporous Aluminosilicate Matrices. *J. Phys. Chem. B* **2001**, *105*, 7414−7423.

(14) Selvam, P.; Dapurkar, S. E.; Badamali, S. K.; Murugasan, M.; Kuwano, H. Coexistence of Paramagnetic and Superparamagnetic Fe (III) in Mesoporous MCM-41 Silicates. *Catal. Today* **2001**, *68*, 69−74.

(15) Cuello, N. I.; Elías, V. R.; Rodriguez Torres, C. E.; Crivello, M. E.; Oliva, M. I.; Eimer, G. A. Development of Iron Modified MCM-41 as Promising Nano-Composites with Specific Magnetic Behavior. *Microporous Mesoporous Mater.* **2015**, *203*, 106−115.

(16) Cano, L. A.; Bengoa, J. F.; Stewart, S. J.; Mercader, R. C.; Marchetti, S. G. Synthesis of Hematite Nanowires using a Mesoporous Hard Template. *Hyperfine Interact.* **2010**, *195*, 93−98.

(17) Srinivasu, P.; Suresh, K.; Datt, G.; Abhayankar, A. C.; Rao, P. N.; Kantam, M. L.; Bhargava, S. K.; Tang, J.; Yamauchi, Y. Ordered

Mesoporous Ferrosilicate Materials with Highly Dispersed Iron Oxide Nanoparticles and Investigation of their Unique Magnetic Properties. *Phys. Chem. Chem. Phys.* **2014**, *16*, 22471−22475.

(18) Ursachi, I.; Vasile, A.; Ianculescu, A.; Vasile, E.; Stancu, A. Ultrasonic-assisted Synthesis and Magnetic Studies of Iron Oxide/ MCM-41 Nanocomposite. *Mater. Chem. Phys.* **2011**, *130*, 1251−1259.

(19) Ryoo, R.; Kim, J. M. Structural Order in MCM-41 Controlled by Shifting Silicate Polymerization Equilibrium. *J. Chem. Soc., Chem. Commun.* **1995**, *7*, 711−712.

(20) Moreno, M. S.; Weyland, M.; Midgley, P. A.; Bengoa, J. F.; Cagnoli, M. V.; Gallegos, N. G.; Alvarez, A. M.; Marchetti, S. G. Highly Anisotropic Distribution of Iron Nanoparticles within MCM-41 Mesoporous Silica. *Micron* **2006**, *37*, 52−56.

(21) Ravel, B.; Newville, M. ATHENA, ARTEMIS, HEPHAESTUS: Data Analysis for X-ray Absorption Spectroscopy using IFEFFIT. *J. Synchrotron Radiat.* **2005**, *12*, 537−541.

(22) Borzi, R. A.; Stewart, S. J.; Punte, G.; Mercader, R. C.; Vasquez-Mansilla, M.; Zysler, R. D.; Cabanillas, E. D. Magnetic Interactions in Hematite Small Particles obtained by Ball Milling. *J. Magn. Magn. Mater.* **1999**, *205*, 234−240.

(23) Mørup, S.; Bødker, F.; Hendriksen, P. V.; Linderoth, S. Spin-glass-like Ordering of the Magnetic Moments of Interacting Nanosized Maghemite Particles. *Phys. Rev. B: Condens. Matter Mater. Phys.* **1995**, *52*, 287−294.

(24) Clausen, B.; Topsøe, H.; Mørup, S. Preparation and Properties of Small Silica-Supported Iron Catalyst Particles: Influence of Reduction Procedure. *Appl. Catal.* **1989**, *48*, 327−340.

(25) Bean, C. P.; Livingston, J. D. Superparamagnetism. *J. Appl. Phys.* **1959**, *30*, S120−S129.

(26) Zeleňáková, A.; Kováč, J.; Zeleňák, V. Magnetic Properties of Fe$_2$O$_3$ Nanoparticles Embedded in Hollows of Periodic Nanoporous Silica. *J. Appl. Phys.* **2010**, *108*, 034323−034327.

(27) Tadic, M.; Markovic, D.; Spasojevic, V.; Kusigerski, V.; Remskar, M.; Pirnat, J.; Jaglicic, Z. Synthesis and Magnetic Properties of Concentrated α-Fe2O3 Nanoparticles in a Silica Matrix. *J. Alloys Compd.* **2007**, *441*, 291−296.

(28) Serna, C. J.; Morales, M. P. Maghemite (γ-Fe$_2$O$_3$): A Veratile Magnetic Colloidal Material, In *Surface and Colloid Science*; Matijevic, E., Borkovec, M., Eds.; Kluwer Academic/Plenum Publishers: New York, 2004; Vol. *17*, Chapter 2, pp 27−81.

(29) Baaziz, W.; Pichon, B. P.; Fleutot, S.; Liu, Y.; Lefevre, C.; Greneche, J. M.; Toumi, M.; Mhiri, T.; Begin-Colin, S. Magnetic Iron Oxide Nanoparticles: Reproducible Tuning of the Size and Nanosized-dependent Composition, Defects, and Spin Canting. *J. Phys. Chem. C* **2014**, *118*, 3795−3810.

(30) Fiorani, D.; Testa, A. M.; Lucari, F.; D'Orazio, F.; Romero, H. Magnetic Properties of Maghemite Nanoparticle Systems: Surface Anisotropy and Interparticle Interaction Effects. *Phys. B* **2002**, *320*, 122−126.

(31) Delahaye, E.; Escax, V.; El Hassan, N.; Davidson, A.; Aquino, R.; Dupuis, V.; Perzynski, R.; Raikher, Y. L. Nanocasting": using SBA-15 Silicas as Hard Templates to obtain Ultrasmall Monodispersed γ-Fe$_2$O$_3$ Nanoparticles. *J. Phys. Chem. B* **2006**, *110*, 26001−26011.

(32) Pisane, K. L.; Despeaux, E. C.; Seehra, M. S. Magnetic Relaxation and Correlating Effective Magnetic Moment with Particle Size Distribution in Maghemite Nanoparticles. *J. Magn. Magn. Mater.* **2015**, *384*, 148−154.

(33) Millan, A.; Urtizberea, A.; Silva, N. J. O.; Palacio, F.; Amaral, V. S.; Snoeck, E.; Serin, V. Surface Effects in Maghemite Nanoparticles. *J. Magn. Magn. Mater.* **2007**, *312*, L5−L9.

(34) Stearns, M.; Cheng, Y. Determination of Para-and Ferromagnetic Components of Magnetization and Magnetoresistance of Granular Co/Ag Films. *J. Appl. Phys.* **1994**, *75*, 6894−6899.

(35) Ali, M.; Adie, P.; Marrows, C. H.; Greig, D.; Hickey, B. J.; Stamps, R. L. Exchange Bias Using a Spin Glass. *Nat. Mater.* **2007**, *6*, 70−75.

(36) Mizrahi, M.; Cabrera, A. F.; Stewart, S. J.; Desimoni, J. Effects of Coexisting Spin Disorder and Antiferromagnetism on the Magnetic Behavior of Nanostructured (Fe79Mn21)$_{1−x}$Cu$_x$ Alloys. *J. Appl. Phys.* **2014**, *115*, 213904−213910.

(37) Mydosh, J. A.; *Spin Glass, An Experimental Introduction*; Taylor & Francis: London, 1993; pp 65−67.

(38) Gadalla, A. M.; Yu, H.-F. Thermal Decomposition of Fe (III) Nitrate and its Aerosol. *J. Mater. Res.* **1990**, *5*, 1233−1236.

(39) Navrotsky, A.; Mazeina, L.; Majzlan, J. Size-driven Structural and Thermodynamic Complexity in Iron Oxides. *Science* **2008**, *319*, 1635−1638.

(40) Del Bianco, L.; Fiorani, D.; Testa, A. M.; Bonetti, E.; Signorini, L. Field-Cooling Dependence of Exchange Bias in a Granular System of Fe Nanoparticles Embedded in an Fe Oxide Matrix. *Phys. Rev. B: Condens. Matter Mater. Phys.* **2014**, *70*, 052401-1−052401-4.

(41) Dormann, J. L.; Fiorani, D.; Tronc, E. Magnetic Relaxation in Fine-Particle Systems. *Adv. Chem. Phys.* **1997**, *98*, 283−494.

(42) Ibrahim, M. M.; Darwish, S.; Seehra, M. S. Nonlinear Temperature Variation of Magnetic Viscosity in Nanoscale FeOOH Particles. *Phys. Rev. B: Condens. Matter Mater. Phys.* **1995**, *51*, 2955−2959.

(43) Zysler, R. D.; Fiorani, D.; Testa, A. M. Investigation of Magnetic Properties of Interacting Fe$_2$O$_3$ Nanoparticles. *J. Magn. Magn. Mater.* **2001**, *224*, 5−11.

(44) Iglesias, O.; Badia, F.; Labarta, A.; Balcells, Ll. Energy Barrier Distributions in Magnetic Systems from the Tln (t/τ0) Scaling. *Z. Phys. B: Condens. Matter* **1996**, *100*, 173−178.

(45) Labarta, A.; Iglesias, O.; Balcells, Ll.; Badia, F. Magnetic Relaxation in Small-Particle Systems: ln(t/τ0) Scaling. *Phys. Rev. B: Condens. Matter Mater. Phys.* **1993**, *48*, 10240−10246.